Stratosphere-troposphere exchanges of air mass and ozone concentration in the Last Glacial Maximum

Mingcheng Wang[1], Qiang Fu[1], Susan Solomon[2], Becky Alexander[1], and Rachel H. White[3]

[1]Department of Atmospheric Sciences, University of Washington, Seattle, WA, USA

[2]Department of Earth, Atmospheric, and Planetary Sciences, Massachusetts Institute of Technology, Boston, MA, USA

[3]Department of Earth, Ocean and Atmospheric Sciences, University of British Columbia

Corresponding author: Mingcheng Wang (wmingch@uw.edu)

Key points

- Global ozone stratosphere-troposphere exchange decreases by 15-21% in simulations of the Last Glacial Maximum versus preindustrial times
- This decrease is mainly caused by decreased ozone in the extratropical lower stratosphere associated with a weakening of the Brewer-Dobson circulation
- Stratosphere-troposphere ozone exchange in the Last Glacial Maximum is 28% of the tropospheric ozone production rate, as compared to 19% in preindustrial times

Abstract

Stratosphere-troposphere exchange (STE) of ozone represents a significant source term in the tropospheric ozone budget and can impact surface ozone concentrations, tropospheric oxidation capacity, and methane lifetime. Using the Whole Atmosphere Community Climate Model 6, changes in the air mass and ozone STEs in the Last Glacial Maximum (LGM) as compared with preindustrial (PI) climate are investigated. We use dynamic isentropic surfaces that are determined by fitting to the tropical tropopauses as the upper boundary of the lowermost stratosphere in a mass budget approach, a method particularly suitable for estimating air mass and ozone STEs across different climates. Relative to the PI, the magnitude of ozone STE in the LGM is decreased by 14-19%, 18-24%, 18-23%, 16-21%, 15-21% over the Northern hemisphere extratropics, Southern hemisphere extratropics, the tropics, the extratropics, and the globe, respectively. The extratropical and global decreases are mainly caused by decreased ozone in the extratropical lower stratosphere associated with a weakening of Brewer-Dobson circulation, while changes in air mass fluxes play a minor role because the effects of weakening Brewer-Dobson circulation and increased isentropic density partly cancel each other. Analysis of the modelled tropospheric ozone budget indicates that the ozone STE in the LGM is 28% of the tropospheric ozone production rate, as compared to about 9% in the modern climate (year 2000) and 19% in the PI.

Key words: stratosphere-troposphere exchange, ozone, Last Glacial Maximum, WACCM6

1. Introduction

As an important component of the tropospheric ozone budget, the stratosphere-troposphere exchange (STE) of ozone can substantially impact tropospheric ozone concentrations (e.g., Collins et al., 2003, Stohl et al., 2003; Ordóñez et al., 2007; Lin et al., 2015). Using surface ozone measurements and a nudged chemistry-climate model, Lin et al. (2015) showed that stratospheric ozone influx can elevate surface ozone concentrations over the western US to unhealthy levels during the spring season. Stratospheric ozone influx can also impact the tropospheric oxidation capacity and methane lifetime (Fiore et al., 2002; Kentarchos and Roelofs, 2003; Geng et al., 2017). A model study by Kentarchos and Roelofs (2003) showed that ozone STE contributes about 15% to the averaged oxidation capacity in the Northern hemisphere (NH) and up to 40% for some regions.

In response to greenhouse gas induced climate change, climate models consistently project an acceleration of the Brewer-Dobson circulation (BDC) (e.g., Butchart et al., 2006; Li et al., 2008; Lin and Fu, 2013; Butchart et al., 2014; Abalos et al., 2021) and an increase of ozone STE (e.g., Collins et al., 2003; Hegglin and Shepherd, 2009; Hess et al., 2015; Meul et al., 2018; Abalos et al., 2020). Similarly, large differences in the atmospheric composition (e.g., CO_2, CH_4, and N_2O concentrations) as well as the Earth's surface conditions for the Last Glacial Maximum (LGM) compared with the modern climate lead us to expect that the stratosphere and the ozone STE in the LGM will also differ from the modern climate.

Compared to the rich literature covering the current and future climate impacts on ozone STE (e.g., Collins et al., 2003; Hess et al., 2015; Hegglin and Shepherd, 2009; Meul et al., 2018;

Abalos et al., 2020), very little attention has been paid to the ozone STE in the LGM (Murray et al., 2014). The latter could be important in the interpretation of ice-core proxies of atmospheric chemistry (Geng et al., 2017; Yeung et al., 2019) and biological productivity (Luz et al., 1999), which motivates its study. Using the GEOS-Chem chemical transport model (CTM), Murray et al. (2014) found that the stratospheric ozone influx is decreased in the LGM relative to the modern climate. Murray et al. (2014) inferred the stratospheric ozone influx as the residual of tropospheric ozone production, loss, and deposition by assuming a budget closure over a year. They suggested that the BDC and the stratospheric ozone influx in their present-day simulation were overly vigorous, a common issue for CTMs (e.g., Liu et al., 2001).

Using the Whole Atmosphere Community Climate Model version 6 (WACCM6), Fu et al. (2020a) and Wang et al. (2020) investigated the BDC and stratospheric ozone in the LGM. Fu et al. (2020a) showed that the model-simulated BDC in the modern climate agrees well with the reanalysis. They found a slower BDC during the LGM than the modern climate, which is due to a downward shift of the wave breaking associated with the zonal wind changes (Fu et al., 2020a). By transporting stratospheric ozone from the tropics, where it is produced, to the extratropics, the BDC plays an important role in determining the stratospheric ozone distribution (e.g., Butchart, 2014). Wang et al. (2020) found that the lower-stratospheric ozone in the LGM as compared to the preindustrial (PI) climate increases in the tropics and decreases in the extratropics because of a weakening of the BDC. This current study examines the ozone STE in the LGM and its changes as compared to the PI climate.

Various methods have been used to estimate ozone STEs (see Stohl et al., 2003; Schoeberl, 2004; Hsu et al., 2005; Wang and Fu, 2021). In contrast to Murray et al. (2014), the STEs of air mass and ozone concentration in this study are directly quantified using the widely used lowermost stratosphere mass budget approach (e.g., Appenzeller et al. 1996). While this approach cannot isolate the locations of STE events, it can accurately estimate the net mass fluxes of air, ozone, and other species across the tropopause over the NH and Southern hemisphere (SH) extratropics, tropics, and globe – our focus here. This approach is often used as an important constraint and reference to assess estimates obtained with other techniques (e.g., Stohl et al., 2003; Škerlak et al., 2014). Note that the air mass net flux across the tropopause, derived using the mass budget approach (e.g., Appenzeller et al., 1996), is the difference of two much larger opposing one-way fluxes (i.e., stratosphere-to-troposphere and troposphere-to-stratosphere transports). While the magnitude of estimated one-way air mass fluxes depends on the smallest resolved length and time scales (e.g., Wernli and Bourqui, 2002; Hall and Holzer, 2003; Orbe et al., 2012), the air mass net fluxes, especially on seasonal or longer timescales, are not sensitive to the details of resolved near-tropopause phenomena (Holton et al., 1995; Yang et al., 2016). In this study, the net mass fluxes across the tropopause, i.e., the net stratosphere-troposphere exchange, is simply referred to as the stratosphere-troposphere exchange.

In this lowermost stratosphere mass budget approach, the 380 K isentropic surface, lying just above the tropical tropopause, is often used as the upper boundary of the lowermost stratosphere. However, the upper boundary of the lowermost stratosphere is expected to change with the changing tropical tropopause in different climates. Here we deploy the budget approach but use a dynamic upper isentropic surface boundary determined by fitting to the tropical tropopause for

each climate, i.e., a different boundary for the LGM versus PI. We find that the magnitude of the global ozone STE is decreased by 15-21% in the LGM versus PI, mainly due to smaller ozone concentrations in the extratropical lower stratosphere resulting from a weakening of BDC during the LGM. We also show that ozone STE in the LGM is 28% of the tropospheric ozone production rate as compared to 19% in the PI climate.

Sections 2 and 3 describe model experiments and the method used, respectively. The main results are presented in section 4. Section 5 gives the summary and conclusions.

2. Model Experiments

We analyze the simulations from Fu et al. (2020a, 2020b) and Wang et al. (2020), who used WACCM6 with 70 vertical levels up to 140 km and a horizontal resolution of 0.9° latitude by 1.25° longitude (Gettelman et al., 2019). WACCM6 has a realistic, internally generated quasi-biennial oscillation in the stratosphere (Garcia and Richter, 2019; Gettelman et al., 2019; Fu et al., 2020b). The BDC in WACCM6 agrees well with ERA-Interim (Fu et al., 2020a). The WACCM model provides a realistic evolution of the SH springtime ozone hole over the latter half of the twentieth century (Solomon et al., 2015). Relative to previous versions of the WACCM, the updated tropospheric chemistry scheme used in WACCM6 leads to improvements in the tropospheric ozone representation when compared to observations (Emmons et al., 2020).

Four simulations are analyzed in this study, consisting of 1) LGM simulation with prescribed sea surface temperatures (SSTs) derived from models (LGM_{PMIP3}), 2) LGM simulation with the SSTs based on proxy data (LGM_{PROXY}), 3) Preindustrial climate simulation (PI), and 4) modern

climate simulation (MC). The MC simulation is used here to compare with previous observational and modeling studies (e.g., Gettelman et al., 1997; Olsen et al., 2004; Hsu et al., 2005; Olsen et al., 2013; Yang et al., 2016; Wang and Fu, 2021), providing confidence in the WACCM6-derived STEs. We analyze simulations from Year 11-40, with the first 10 years discarded for spin-up. The greenhouse gas concentrations and orbital parameters in the simulations correspond to the LGM, PI, and MC conditions (Fu et al., 2020a, 2020b; Wang et al., 2020). For the PI (MC) simulation, the observed climatology SSTs and sea ice of years 1870-1890 (1980-2000) with a seasonal cycle (Rayner et al., 2003) are used. The SSTs and sea ice in LGM_{PMIP3} are taken from the model differences between the LGM and MC simulations plus corresponding observed SSTs/sea ice in the MC (Fu et al., 2020a, 2020b). For LGM_{PROXY}, the SSTs are taken from the MARGO proxy data (Kucera et al., 2005), and with the same sea ice as in LGM_{PMIP3}. WACCM6 is coupled with the CLM4.0 land model (Oleson et al., 2010) and utilizes the CLM4.0 LGM lower boundary conditions from the CESM Paleo Working group (Brady et al., 2013). The ice sheet topography in the LGM simulations is from Abe-Ouchi et al. (2015). More details of the model setup are provided in Fu et al. (2020a, 2020b) and Wang et al. (2020).

3. Analysis method

Figure 1 shows a schematic of the components involved in the air mass and ozone STEs for the methods of (a) Appenzeller et al. (1996), (b) Wang and Fu (2021), and (c) the present study. In the lowermost stratosphere mass budget approach, the 380 K isentropic surface just lying above the tropopause in the tropics (e.g., Holton et al., 1995), is often used as the upper boundary of the lowermost stratosphere (e.g., Appenzeller et al., 1996; Schoeberl 2004; Olsen et al., 2004; Olsen

et al., 2013; Yang et al., 2016; Wang and Fu, 2021). However, for different climates, the upper boundary of the lowermost stratosphere is also expected to change with the tropical tropopause. In this study, we propose the dynamic upper isentrope method (Figure 1c) that uses a dynamic isentropic surface as the upper boundary of the lowermost stratosphere, which is determined by fitting to the tropical lapse rate tropopauses (WMO, 1957) in different climates. This is distinctly different from a constant 380 K isentrope used in Appenzeller et al. (1996) (Figure 1a) and Wang and Fu (2021) (Figure 1b). The dynamic upper isentropic surface (red solid line in Figure 1c) is determined by minimizing the difference between the isentropic levels ranging from 360 K to 390 K with a 1 K interval and the lapse rate tropopause over the regions equatorward of the latitudes with zero tropopause diabatic heating. These fitted upper isentropic surfaces are 373 K, 370 K, 361 K, 365 K in the MC, PI, LGM_{PMIP3}, and LGM_{PROXY}, respectively. Following Schoeberl (2004) and Wang and Fu (2021), a 3.5 potential vorticity unit (PVU) surface (1 PVU = 10^6 m^2 K kg^{-1} s^{-1}) is used as the extratropical tropopause, and the tropopause at the tropics is the fitted upper isentrope. The regions poleward of the zero diabatic heating at the fitted upper isentrope are defined as the extratropics, while the equatorward regions are defined as the tropics. The light blue shaded regions between the 3.5 PVU tropopause and the upper isentropic surface constitute the extratropical lowermost stratosphere (Figure 1c). The dynamic upper isentrope method avoids the gap between the tropical tropopause and upper isentropic surface in the tropics (i.e., the light red shading in Figure 1b) and thus the horizontal transport between the tropical and extratropical lowermost stratospheres. The latter is not part of the STEs (see Schoeberl (2004) and Wang and Fu (2021) for details). The comparison of air mass and ozone STEs between Wang and Fu (2021) and dynamic upper isentrope methods is discussed in the Appendix for the modern climate.

The definition of extratropics/tropics boundaries has little impact on the estimated global STEs, but does have a large impact on the STE partitioning over the NH extratropics, SH extratropics, and the tropics. The annual- and zonal-mean extratropics/tropics boundaries in the dynamic upper isentrope method are similar in all climates, and are located at about 32-33° N and 31-32° S. Different from the dynamic upper isentrope method, Appenzeller et al. (1996) used a constant isentropic surface of 380 K and defined the extratropics/tropics boundaries as the cross point between the PVU tropopause and 380 K isentrope (Figure 1a). The derived annual- and zonal-mean extratropics/tropics boundaries are about 17° N, 15° N, 11° N, 11° N in the NH, and 18° S, 16° S, 11° S, 11° S in the SH for the MC, PI, LGM_{PMIP3}, and LGM_{PROXY}, respectively. The equatorward shifts of extratropics/tropics boundaries in the colder climate here are due to a lower tropopause (see Figure 2 in Wang et al., 2020) but higher 380 K isentrope (not shown). Therefore, a constant 380 K upper isentropic surface would lead to an apparent reduction in the downward air mass and ozone flux over the extratropics in the cold climate as compared with MC, which is not related to the change in climate, but rather to the change in defined extratropics/tropics boundaries. This is because more portions of the upwelling region between ~30° N/S and the defined boundary latitudes are included, which then partly compensates the downward flux poleward of about 30° N/S (see Figure 1a).

The air mass flux across the tropopause (F_{trop}) can be calculated from the sum of the diabatic air mass flux across the fitted upper isentrope (F_{upper}) and the rate of change in the lowermost stratosphere air mass ($\frac{dM}{dt}$),

$$F_{trop} = F_{upper} + \frac{dM}{dt} \quad (1)$$

The diabatic flux across the upper isentrope can be derived from $\iint Q\sigma\, dA$, where $Q = R\frac{\theta}{T}$ is the diabatic heating rate, $\sigma = -g^{-1}\frac{\partial p}{\partial \theta}$ is isentropic density, R is the radiative heating rate, θ is the potential temperature, T is the temperature, p is pressure, g is the gravitational acceleration constant, and A is the area over the NH extratropics, SH extratropics, and tropics. Over the tropics where the tropopause is the fitted upper isentropic surface, $F_{trop} = F_{upper}$. The summation of the fluxes over the NH and SH extratropics is hereafter referred to as the flux over the extratropics, and the summation of the fluxes over the extratropics and tropics as that over the globe. In Equation 1, F_{upper} is positive for the upwelling flux while F_{trop} is positive for the flux entering the stratosphere (lowermost stratosphere) over the tropics (extratropics). Schoeberl (2004) extended Appenzeller et al. (1996) by further dividing F_{trop} into diabatic ($F_{trop\text{-}d}$) and adiabatic ($F_{trop\text{-}a}$) components. $F_{trop\text{-}d}$ is calculated using the same method as the diabatic flux across the upper isentrope but on the tropopause surface. The adiabatic flux is then the residual of F_{trop} and $F_{trop\text{-}d}$.

Similarly, the net ozone flux across the tropopause ($F_{trop}^{O_3}$) can be derived from the diabatic ozone flux at the fitted upper isentropic surface, $F_{upper}^{O_3}$, and the rate of change of the ozone mass in the lowermost stratosphere, $\frac{dO_3}{dt}$, with an added term for ozone net chemical source (CTO3),

$$F_{trop}^{O_3} = F_{upper}^{O_3} + \frac{dO_3}{dt} - CTO3 \quad (2)$$

where CTO3 is calculated by integrating ozone net chemical sources at every level and grid point within the lowermost stratosphere. As in Equation 1, Equation 2 is applied to the NH and SH

extratropics to derive ozone STEs. In the tropics, $F_{trop}^{O_3} = F_{upper}^{O_3}$. Likewise, the tropopause net ozone flux ($F_{trop}^{O_3}$) over the extratropics can be separated into tropopause diabatic ($F_{trop-d}^{O_3}$) and adiabatic ozone fluxes ($F_{trop-a}^{O_3}$).

The derived global air mass fluxes at the upper isentrope may not be zero. Therefore, following Olaguer et al. (1992) and Rosenlof (1995), the diabatic heating rate at the fitted upper isentrope is adjusted by subtracting or adding a constant to produce a global zero net air mass flux for each month. Hereafter, 'diabatic heating' refers to the diabatic heating after the adjustment, unless otherwise indicated. The following results are based on monthly data, and the results are quite similar to those derived using daily data (not shown).

4. Results

4.1 Air mass and ozone STEs

The seasonal evolution of air mass and ozone STEs during the PI are shown in Figure 2, based on the dynamic upper isentrope method. Tables 1 and 2 give the annual mean air mass and ozone fluxes during the PI, LGM_{PMIP3}, and LGM_{PROXY}, with relative differences for the LGM_{PMIP3} and LGM_{PROXY} versus PI shown in the parentheses. Note that we show the negative of ozone net chemical source in the lowermost stratosphere (−CTO3) in Table 2, Table 3, Figure 2, Table S1, Figure S1, and Figure S2. The tropopause net air mass fluxes during the MC as compared to PI (Table S1a versus Table 1a) are increased by 4%, 1%, and 3% over the NH extratropics, SH extratropics, and the tropics, which are all statistically significant. For reference, the interannual variabilities of tropopause net air mass fluxes, measured by one standard deviation of annual-mean values divided by the climatic mean, during the MC (PI) are 1.5% (1.9%), 2.6% (2.8%),

and 1.2% (1.6%) over the NH extratropics, SH extratropics, and the tropics, respectively. Using the Appenzeller et al. (1996) approach with a constant 380 K upper isentropic surface, by contrast, the air mass fluxes for MC versus PI are increased by ~30% over all regions including NH and SH extratropics, and the tropics (not shown). These large increases are mainly because of the poleward shifts of the extratropics/tropics boundary latitudes from ~15° N/S during the PI to ~18° N/S during the MC, which are largely a matter of definition. Using the Wang and Fu (2021) method, the tropopause net air mass fluxes for the MC versus PI are increased by ~ 10% over the NH and SH extratropics, and the tropics (not shown). Note that the gap between the tropical tropopause and 380 K in the Wang and Fu (2021) approach would decrease in a warming climate, which would affect the estimates of the STE changes over the extratropics and tropics. Below we examine the STE changes during the LGM versus PI based on the dynamic upper isentrope method.

Compared to the PI, the tropopause net air mass fluxes in the LGM are decreased by 0.3-2% over the SH extratropics, but increased by 5-7% and 2-4% over the NH extratropics and the tropics (Table 1). The interannual variabilities of tropopause net air mass fluxes during the LGM_{PMIP3} (LGM_{PROXY}) are 2.4% (2%), 1.8% (2.2%), and 1.4% (1.4%) over the NH extratropics, SH extratropics, and the tropics, respectively. As shown in Figure 3a, the magnitudes of diabatic heating are generally decreased, associated with a weakening BDC for the LGM versus PI. The effect of the weakening BDC, however, is canceled out by increased isentropic density (Figure 3b), leading to increases in air mass STEs in the NH extratropics and the tropics. For the LGM versus PI, the tropopause diabatic air mass fluxes are increased over the NH extratropics and the tropics, but the changes are inconclusive over other regions (Table 1). The changes in

tropopause adiabatic air mass fluxes for the LGM versus PI are inconclusive in all regions (Table 1).

The tropopause net ozone fluxes are decreased by 14-19%, 18-24%, 18-23%, 16-21%, 15-21% over the NH and SH extratropics, the tropics, the extratropics, and the globe, for the LGM versus PI (Table 2). The reduction in tropopause net ozone fluxes in the colder climate is largely due to the reductions of ozone concentration over all regions, driven by different factors in the tropics versus the extratropics (explained in detail in Section 4.2 below). Like the tropopause net ozone fluxes, the tropopause diabatic ozone fluxes are decreased by 13-24% over all regions for the LGM versus PI. The tropopause adiabatic ozone fluxes are small (Olsen et al., 2004; Wang and Fu 2021), and their changes in the LGM as compared to PI are inconclusive (Table 2). In the extratropical lowermost stratosphere, there are net ozone chemical sinks, which are larger in the LGM as compared to the PI (Table 2); this may be related to the increased stratospheric temperature and thus faster ozone loss reaction rates during the LGM (Wang et al., 2020).

Although the approach of Wang and Fu (2021) might not be suitable to derive the changes in air mass and ozone STEs over extratropics and tropics for different climates, it can derive the global STEs accurately (Wang and Fu, 2021). Table 3 shows the global ozone STEs in the PI, LGM_{PMIP3}, and LGM_{PROXY} using the Wang and Fu (2021) method. There is excellent agreement for the global tropopause net ozone fluxes using the dynamic upper isentrope method (i.e., 367, 291, and 312 Tg year^{-1} during the PI, LGM_{PMIP3}, and LGM_{PROXY}, respectively) and Wang and Fu (2021) method (i.e., 367, 287, and 308 Tg year^{-1}, correspondingly). The relative changes in the

global tropopause net ozone fluxes during the LGM versus PI from the two methods are almost identical.

We also examine the changes in ozone STEs during the MC versus PI using the dynamic upper isentrope method (Table S1c versus Table 2a). The tropopause net ozone fluxes are increased by 25%, 54%, and 9% over the NH extratropics, the tropics, and the extratropics, but decreased by 13% and 1% over the SH extratropics and the globe. The decreased ozone STE over the SH extratropics is due to a large ozone depletion there in the MC (Solomon, 1999).

4.2 Causes of STE changes during the LGM versus PI

The annual-mean tropopause net air mass and ozone fluxes and changes are well approximated by the annual-mean diabatic fluxes and changes across the fitted upper isentropic surfaces (Tables 1 and 2). Here we examine the role of individual factors, including the diabatic heating, isentropic density, extratropics/tropics boundary, and ozone concentrations, in the changes of annual-mean diabatic air mass and ozone fluxes across the upper isentropic surface during the LGM versus PI.

Figure 3 shows the latitudinal distributions of annual-mean zonal-mean diabatic heating, isentropic density, ozone mass mixing ratio at the fitted upper isentrope during the PI, LGM_{PMIP3}, and LGM_{PROXY} (upper panel), and the corresponding differences for the LGM_{PMIP3} and LGM_{PROXY} versus PI (lower panel). The diabatic heating is positive over the tropics and negative over the extratropics (Figure 3a). Relative to the PI, the change of diabatic heating in the LGM is generally the reverse of the climatology (Figure 3e), consistent with a weakening of

the BDC in the LGM (Fu et al., 2020a). The reduced diabatic cooling (i.e., weakening of BDC) around 40° N -50° N is alleviated in the LGM_{PMIP3} versus PI, and the diabatic cooling over this region is even enhanced (i.e., stronger BDC) in the LGM_{PROXY} versus PI; this may be related to the local intensification of the BDC induced by the Laurentide ice sheet (Fu et al., 2020a; Wang et al., 2020).

Figure 4 is the same as Figure 3, but for longwave and shortwave diabatic heating. No adjustment is applied to the longwave and shortwave heating rates. The latitudinal dependence in the shape of changes in diabatic heating for LGM versus PI is similar to that associated with the longwave heating, while the changes in shortwave heating shift the diabatic heating down by ~0.05 K day^{-1} (Figure 4). Gettelman et al. (2004) examined the importance of various radiatively active gases for the radiation balance at the tropical tropopause layer, and found that water vapor makes the largest contribution to the radiation balance there, while carbon dioxide and ozone also play some role (see Figure 5 in Gettelman et al., 2004). As shown in Wang et al. (2020), the stratospheric water vapor in the LGM compared to the PI is decreased everywhere because of the lower methane concentration and colder tropopause temperature in the LGM. Therefore, the reduced longwave cooling rate at the extratropics for the LGM versus PI (Figure 4c) is largely due to the reduced longwave cooling by water vapor. The reduced longwave cooling by water vapor for the LGM versus PI leads to increased longwave *heating* in the tropics (Figure 4c). Relative to the PI, the shortwave heating is decreased in the LGM everywhere, with small latitudinal variations (Figure 4d), due to lower concentrations of water vapor and carbon dioxide in the LGM.

For the LGM versus PI, the isentropic density is increased at all latitudes (Figures 3b and 3f), which is due to the lower upper isentropic surface (Figure 3d and 3h) corresponding to the lower tropical tropopause in the LGM (see also Figure 2 in Wang et al., 2020). The ozone concentrations for the LGM versus PI are decreased at all latitudes (Figures 3c and 3g). The weakening of the BDC (Fu et al., 2020a; Wang et al., 2020) can explain the decreases of ozone concentrations in the lower stratosphere over the extratropics. In the tropics, the reduced ozone concentrations near the tropopause are due to decreased tropospheric ozone production (Wang et al., 2020).

We quantify the changes in air mass and ozone STEs due to changes in extratropics/tropics boundary, isentropic density, diabatic heating, and ozone concentrations following the method in Wang and Fu (2021). For LGM_{PMIP3} versus PI, we first replace PI extratropics/tropics boundary with LGM_{PMIP3} extratropics/tropics boundary, but retain the PI isentropic density, diabatic heating, and ozone. Then we further replace PI isentropic density with LGM_{PMIP3} isentropic density but retain PI diabatic heating and ozone. We continue replacing PI diabatic heating with LGM_{PMIP3} diabatic heating but retain PI ozone. Finally, we replace the PI ozone with the LGM_{PMIP3} ozone (i.e., using all fields from LGM_{PMIP3}). The flux differences between the two calculations are referred to as the flux differences due to the variable replaced. The order of the replacement only has a minor impact on the results (not shown). Note that this approach neglects the interactions among the variables considered (e.g., the coupling between changes in ozone and diabatic heating). The same calculation for the LGM_{PROXY} versus PI is also performed. Different from Wang and Fu (2021), we do not make a diabatic heating adjustment after replacing the PI

diabatic heating or isentropic density with fields in the LGM since we investigate the STE changes between different climates.

Figure 5 shows that for the LGM versus PI, the changes in air mass fluxes over the NH extratropics (Figure 5a) are dominated by the increases associated with increased isentropic density, compensated slightly by the decreases associated with increased diabatic heating (i.e., a weakening of the BDC). On the other hand, there are slight decreases in air mass fluxes over the SH extratropics for the LGM versus PI (Figure 5c). This is because of the large cancellation between the decreases due to diabatic heating changes and the increases associated with isentropic density. The cancellation between the diabatic heating and isentropic density may be due to the tight coupling between the diabatic heating and temperature in the lowermost stratosphere. Over the tropics, there are increases in air mass fluxes for the LGM versus PI due to the increases in isentropic density (Figure 5e). The changes in extratropics/tropics boundaries also play some role, which leads to a slight decrease in air mass fluxes over all regions (Figures 5a, 5c, and 5e).

The relative changes in ozone STEs are negative over all regions for the LGM versus PI, mainly due to the decreased ozone concentrations (Figures 5b, 5d, 5f, 5g). The decreased ozone in the extratropical lower stratosphere (Wang et al., 2020) leads to less ozone flux from the stratosphere to the troposphere over extratropics (Table 2). On the other hand, the decreased ozone at the tropical tropopause results in less ozone flux from the troposphere to the stratosphere over the tropics (Table 2). These two terms have opposite contributions to the changes in the global tropospheric ozone budget for the LGM versus PI, but the decreased extratropical ozone

dominates. Thus, the decreased net ozone fluxes from the stratosphere to the troposphere over the globe are mainly caused by the weakening of the BDC through its impact on the ozone concentrations in the extratropical lower stratosphere (Table 2). The contributions to the ozone STEs from changes in the extratropics/tropics boundaries are generally small (Figures 5b, 5d, and 5f). As expected, the extratropics/tropics boundaries have no impact on the global ozone STEs (Figure 5g).

4.3 Tropospheric ozone budget

Ozone STE is a crucial component for the tropospheric ozone budget (e.g., Stohl et al., 2003; Bates and Jacob, 2020; Griffiths et al., 2020). Table 4 shows the global tropospheric ozone burden, ozone lifetime, ozone chemical production and loss rate, ozone deposition, and ozone STEs in all climate simulations. The residuals of tropospheric ozone production, loss, deposition, and ozone STEs are also shown in Table 4. The tropospheric ozone lifetime in Table 4 is calculated by dividing the tropospheric ozone burden by the total ozone losses (chemical loss plus deposition). The tropopause (i.e., a combination of 3.5 PVU tropopause and the fitted upper isentrope) is used as the upper boundary of the troposphere for the vertical tropospheric column integration.

In the MC, the tropospheric ozone burden, ozone production rate, ozone loss rate, ozone deposition flux, and tropospheric ozone lifetime are all in the range reported by previous studies (e.g., Young et al., 2013; 2018). The ozone STE over the extratropics in the MC (484 Tg year^{-1} in Table S1c) is quite similar to the stratospheric ozone influx (469-479 Tg year^{-1}) obtained using the CESM2 simulations for the year 2013 (Emmons et al., 2020) (see their Table 3). Note that

the residuals of the tropospheric ozone budget (i.e., summation of ozone production rate, loss, deposition, and ozone STE) in Emmons et al. (2020) are 217-287 Tg year^{-1}, quite close to our residual (i.e., 220 Tg year^{-1}) without considering the tropical upward ozone flux in the MC. By contrast, the residual of the tropospheric ozone budget in the MC becomes much smaller (i.e., 100 Tg year^{-1}) after considering the tropical upward ozone flux (Wang and Fu, 2021).

In the PI simulation, the tropospheric ozone burden, tropospheric ozone production rate, ozone loss rate, and ozone deposition flux are all much smaller than the MC. Such a result is in line with past studies, showing a significant increase of tropospheric ozone since the preindustrial because of higher photochemical ozone production related to anthropogenic emission of NO_x, hydrocarbons, and CO from the combustion of fossil fuels (e.g., Young et al., 2013). During the LGM, the tropospheric ozone burden, tropospheric ozone production rate, ozone loss rate, and ozone deposition flux are 135-137 Tg, 1071-1086 Tg year^{-1}, 1090-1136 Tg year^{-1}, 315-318 Tg year^{-1}, respectively. The decreased tropospheric ozone burden, and ozone production and loss rates in the LGM versus PI may be related to the reduced surface emissions of ozone precursor gases (Wang et al., 2020). The reduced ozone deposition flux may be related to both surface land types (e.g., widespread ice sheets in the NH) and a decreased tropospheric ozone burden. On the relative contribution of ozone STE to the tropospheric ozone budget, Table 4 shows that ozone STE in the LGM is ~28% of the tropospheric ozone production rate, as compared to only 9% in the modern climate (year 2000) and 19% in the PI. The tropospheric ozone lifetimes are 34-35 days in the LGM, which are longer than the PI and MC, consistent with Murray et al. (2014). The residuals of the tropospheric ozone budget are positive for MC but negative for PI and LGM, which have a magnitude less than 100 Tg/yr in all simulations (Table 4). The non-zero

residuals may be related to the fast chemical cycles between ozone and hydrogen oxide (HO_x) and will be further investigated in the future.

5. Conclusion and discussion

This study investigates air mass and ozone STEs in the LGM versus PI based on WACCM6 simulations using the lowermost stratosphere mass budget approach with dynamic upper isentropic surfaces obtained by fitting to tropical tropopauses in different climates. Our analysis shows that the budget approach with a fixed upper isentropic surface (e.g., 380 K) is not suitable for examining the STE changes in response to climate changes.

As compared to the PI, the tropopause net air mass flux is decreased by 0.3-1.5% over the SH extratropics, but increased by 5-7% over the NH extratropics, and 2-4% over the tropics in the LGM. The relatively small changes in air mass fluxes and their different signs over different regions are due to the compensating effects of changes in diabatic heating related to a weakening of the BDC, along with increased isentropic density related to the lower tropopause in the LGM. The ozone fluxes for the LGM versus PI are decreased by 14-19%, 18-24%, 18-23%, 16-21%, 15-21% over the NH extratropics, SH extratropics, the tropics, the extratropics, and the globe, respectively, mainly caused by decreased ozone concentrations at the fitted upper isentrope over all latitudes. Over the extratropics, the decreased ozone concentrations for the LGM versus PI are caused by the weakening of BDC, while the decreased ozone over the tropics is due to a decreased tropospheric ozone production related to the reduced surface emissions of ozone precursor gases. The contribution of the ozone STE change over the extratropics and that over the tropics to the global tropospheric ozone budget have opposite signs, but the former dominates.

The reduced ozone STE source to the global tropospheric ozone budget in the LGM versus PI is thus mainly caused by decreased ozone concentrations over the extratropics related to a weakening of BDC. The impact of the BDC through air mass flux changes plays only a small role in the ozone STE changes. The contributions from extratropics/tropics boundary changes are generally small for both air mass and ozone STEs.

On the tropospheric ozone budget, relative to the PI, the tropospheric ozone burden, ozone production rate, ozone loss rate, and ozone deposition in the LGM are all decreased, and the tropospheric ozone lifetime in the LGM is increased, in line with Murray et al. (2014). It is also shown that ozone STE in the LGM is ~28% of the tropospheric ozone production rate, as compared to the fraction of 9% in the modern climate (year 2000) and 19% in the PI.

Appendix: Various lowermost stratosphere mass budget approaches

Following Schoeberl (2004), Wang and Fu (2021) used the combined tropopause (i.e., 3.5 PVU tropopause over the extratropics but lapse rate tropopause over the tropics, with the transition latitudes identified where the 3.5 PVU tropopause crosses the lapse rate tropopause) along with a 380 K isentropic surface as the upper boundary of the lowermost stratosphere (see Figure 1b). Wang and Fu (2021) estimated the STE of air masses and ozone concentrations based on reanalysis and observations over both the extratropics and the tropics. They defined the boundary latitudes between the extratropics and tropics as those where the tropopause diabatic heating is zero (white vertical lines in Figure 1b), which occurs at ~30° N/S. Wang and Fu (2021) showed that the global ozone STE averaged over 2007–2010 is about 350 Tg year^{-1}. A key finding was

that the tropical upward ozone flux compensates ~35% of the extratropical downward ozone fluxes and should not be neglected.

As noted in Wang and Fu (2021), the derived net fluxes across the tropopause over the extratropics and tropics using the Schoeberl (2004) method include the exchanges of air mass and ozone across the gaps between the tropopause and 380 K at the extratropics/tropics boundary latitudes (white vertical lines in Figure 1b). The strong anticyclonic vortex in the upper troposphere and lower stratosphere associated with the Asian summer monsoon can contribute to this horizontal transport between the extratropics and the tropics (Randel et al., 2010; Randel and Jensen, 2013). Those horizontal fluxes across the gaps, however, do not have any impact on the estimated global air mass and ozone STEs (Wang and Fu, 2021). On the other hand, in Appenzeller et al. (1996) method (Figure 1a), the boundaries between the extratropics and tropics are the cross points between the 3.5 PVU tropopause and the 380 K isentrope that is considered as the tropical tropopause, which are at ~20° N/S. Thus, there are no gaps between 380 K and the tropical tropopause in the Appenzeller et al. (1996) method. Wang and Fu (2021) showed that there is little difference in estimated global ozone STEs using the Schoeberl (2004) versus Appenzeller et al. (1996) methods, but the partition of the global ozone STE between the extratropics and tropics does depend on the methods used. This is mainly because of the differences in the extratropics/tropics boundary latitudes between the two methods. The exchanges of air mass and ozone across the gaps between the tropopause and 380 K in the Schoeberl (2004) approach, which is not part of the STEs, also impact the partitioning of the global ozone STE over the extratropics and tropics.

Table S1 shows the annual-mean air mass and ozone fluxes in the MC using the dynamic upper isentrope method and those following the Wang and Fu (2021) method, with the corresponding seasonal cycle shown in Figures S1 and S2. The MC results using the Wang and Fu (2021) method (Table S1b and S1d, Figure S2) are in good agreement with reanalysis and observational results using the same method (Tables 1, 2, and Figure 2 in Wang and Fu, 2021), except for a smaller seasonal variation of tropopause net ozone flux over the SH extratropics in the WACCM6 MC simulation (Figure S2d). In accordance with earlier studies (e.g., Olsen et al., 2004; Hegglin and Shepherd, 2009), the CTO3 in the lowermost stratosphere over the NH extratropics (~4 Tg year^{-1}) is negligible (Table S1d). On the other hand, we find a larger ozone chemical sink of ~25 Tg year^{-1} over the SH extratropics in the MC because of ozone depletion there (Solomon, 1999). It is also interesting to note an ozone chemical source of ~22 Tg year^{-1} over the tropics, but the CTO3 term over the globe is small (i.e., 7 Tg year^{-1}) (Table S1d).

The magnitudes of annual mean of tropopause net air mass fluxes in the MC based on the dynamic upper isentrope method are larger than those using the Wang and Fu (2021) method (Table S1a versus Table S1b). This is because of the lower fitted upper isentropic surface (i.e., 373 K versus 380 K). On the other hand, the tropopause net ozone fluxes over all regions from the two methods agree well (Table S1c versus Table S1d). The seasonal evolutions of air mass and ozone STEs in the MC using the two methods are also quite similar (Figure S1 versus Figure S2). See Wang and Fu (2021) for the comparison of the Appenzeller et al. (1996) and the Wang and Fu (2021) methods.

Acknowledgments: This research was supported by NSF Grant AGS-1821437 and NASA Grant 80NSSC18K1031. SS gratefully acknowledges support by NSF AGS-1848863. We would like to acknowledge high-performance computing support from Cheyenne (doi:10.5065/D6RX99HX) provided by NCAR's Computational and Information Systems Laboratory, sponsored by the National Science Foundation, for the analyses presented in this study and for the data management, storage, and preservation. The authors wish to thank the International Space Science Institute (ISSI) Tropical Width Impacts on the Stratosphere (TWIST) group for their valuable discussions and feedback on this work. Data used in this study can be obtained from the University of Washington Research Works Archive (through the link http://hdl.handle.net/1773/48135).

Reference

Abalos, M., et al. (2021), The Brewer–Dobson circulation in CMIP6, Atmos. Chem. Phys., 21(17), 13571-13591, doi:10.5194/acp-21-13571-2021.

Abalos, M., et al. (2020), Future trends in stratosphere-to-troposphere transport in CCMI models, Atmos. Chem. Phys., 20(11), 6883-6901, doi:10.5194/acp-20-6883-2020.

Abe-Ouchi, A., et al. (2015), Ice-sheet configuration in the CMIP5/PMIP3 Last Glacial Maximum experiments, Geosci Model Dev, 8(11), 3621-3637, doi:10.5194/gmd-8-3621-2015.

Appenzeller, C., J. R. Holton, and K. H. Rosenlof (1996), Seasonal variation of mass transport across the tropopause, Journal of Geophysical Research: Atmospheres, 101(D10), 15071-15078.

Bates, K. H., and D. J. Jacob (2020), An Expanded Definition of the Odd Oxygen Family for Tropospheric Ozone Budgets: Implications for Ozone Lifetime and Stratospheric Influence, Geophys Res Lett, 47(4), doi:10.1029/2019gl084486.

Brady, E. C., B. L. Otto-Bliesner, J. E. Kay, and N. Rosenbloom (2013), Sensitivity to Glacial Forcing in the CCSM4, J Climate, 26(6), 1901-1925, doi:10.1175/jcli-d-11-00416.1.

Butchart, N. (2014), The Brewer-Dobson circulation, Rev Geophys, 52(2), 157-184, doi:10.1002/2013rg000448.

Butchart, N., et al. (2006), Simulations of anthropogenic change in the strength of the Brewer-Dobson circulation, Clim Dynam, 27(7-8), 727-741, doi:10.1007/s00382-006-0162-4.

Collins, W. J., R. G. Derwent, B. Garnier, C. E. Johnson, M. G. Sanderson, and D. S. Stevenson (2003), Effect of stratosphere-troposphere exchange on the future tropospheric ozone trend, J Geophys Res-Atmos, 108(D12), doi:10.1029/2002jd002617.

Emmons, L. K., R. H. Schwantes, J. J. Orlando, G. Tyndall, D. Kinnison, J. F. Lamarque, D. Marsh, M. J. Mills, S. Tilmes, and C. Bardeen (2020), The Chemistry Mechanism in the Community Earth System Model version 2 (CESM2), J Adv Model Earth Sy, doi:10.1029/2019MS001882.

Fiore, A. M., D. J. Jacob, B. D. Field, D. G. Streets, S. D. Fernandes, and C. Jang (2002), Linking ozone pollution and climate change: The case for controlling methane, Geophys Res Lett, 29(19), doi:10.1029/2002gl015601.

Fu, Q., R. H. White, M. Wang, B. Alexander, S. Solomon, A. Gettelman, D. S. Battisti, and P. Lin (2020a), The Brewer-Dobson Circulation During the Last Glacial Maximum, Geophys Res Lett, 47(5), doi:10.1029/2019gl086271.

Fu, Q., M. Wang, R. H. White, H. A. Pahlavan, B. Alexander, and J. M. Wallace (2020b), Quasi-Biennial Oscillation and Sudden Stratospheric Warmings during the Last Glacial Maximum, Atmosphere-Basel, 11(9), 943.

Garcia, R. R., and J. H. Richter (2019), On the Momentum Budget of the Quasi-Biennial Oscillation in the Whole Atmosphere Community Climate Model, J Atmos Sci, 76(1), 69-87, doi:10.1175/jas-d-18-0088.1.

Geng, L., L. T. Murray, L. J. Mickley, P. Lin, Q. Fu, A. J. Schauer, and B. Alexander (2017), Isotopic evidence of multiple controls on atmospheric oxidants over climate transitions, Nature, 546(7656), 133-+, doi:10.1038/nature22340.

Gettelman, A., P. M. D. Forster, M. Fujiwara, Q. Fu, H. Vomel, L. K. Gohar, C. Johanson, and M. Ammerman (2004), Radiation balance of the tropical tropopause layer, J Geophys Res-Atmos, 109(D7), doi:10.1029/2003jd004190.

Gettelman, A., J. R. Holton, and K. H. Rosenlof (1997), Mass fluxes of O-3, CH4, N2O and CF2Cl2 in the lower stratosphere calculated from observational data, J Geophys Res-Atmos, 102(D15), 19149-19159, doi:10.1029/97jd01014.

Gettelman, A., et al. (2019), TheWhole Atmosphere Community Climate Model Version 6 (WACCM6), J Geophys Res-Atmos, 124(23), 12380-12403, doi:10.1029/2019jd030943.

Griffiths, P. T., J. Keeble, Y. M. Shin, N. L. Abraham, A. T. Archibald, and J. A. Pyle (2020), On the Changing Role of the Stratosphere on the Tropospheric Ozone Budget: 1979-2010, Geophys Res Lett, 47(10), doi:10.1029/2019gl086901.

Hall, T. M., and M. Holzer (2003), Advective-diffusive mass flux and implications for stratosphere-troposphere exchange, *Geophys Res Lett*, *30*(5), doi:https://doi.org/10.1029/2002GL016419.

Hegglin, M. I., and T. G. Shepherd (2009), Large climate-induced changes in ultraviolet index and stratosphere-to-troposphere ozone flux, Nat Geosci, 2(10), 687-691, doi:10.1038/ngeo604.

Hess, P., D. Kinnison, and Q. Tang (2015), Ensemble simulations of the role of the stratosphere in the attribution of northern extratropical tropospheric ozone variability, Atmos Chem Phys, 15(5), 2341-2365, doi:10.5194/acp-15-2341-2015.

Holton, J. R., P. H. Haynes, M. E. McIntyre, A. R. Douglass, R. B. Rood, and L. Pfister (1995), Stratosphere-troposphere exchange, Rev Geophys, 33(4), 403-439.

Hsu, J., M. J. Prather, and O. Wild (2005), Diagnosing the stratosphere-to-troposphere flux of ozone in a chemistry transport model, J Geophys Res-Atmos, 110(D19), doi:10.1029/2005jd006045.

Kentarchos, A. S., and G. J. Roelofs (2003), A model study of stratospheric ozone in the troposphere and its contribution to tropospheric OH formation, J Geophys Res-Atmos, 108(D12), doi:10.1029/2002jd002598.

Kucera, M., A. Rosell-Mele, R. Schneider, C. Waelbroeck, and M. Weinelt (2005), Multiproxy approach for the reconstruction of the glacial ocean surface (MARGO), Quaternary Sci Rev, 24(7-9), 813-819, doi:10.1016/j.quascirev.2004.07.017.

Li, F., J. Austin, and J. Wilson (2008), The strength of the Brewer-Dobson circulation in a changing climate: Coupled chemistry-climate model simulations, J Climate, 21(1), 40-57, doi:10.1175/2007jcli1663.1.

Lin, M. Y., A. M. Fiore, L. W. Horowitz, A. O. Langford, S. J. Oltmans, D. Tarasick, and H. E. Rieder (2015), Climate variability modulates western US ozone air quality in spring via deep stratospheric intrusions, Nature Communications, 6, doi:10.1038/ncomms8105.

Lin, P., and Q. Fu (2013), Changes in various branches of the Brewer-Dobson circulation from an ensemble of chemistry climate models, J Geophys Res-Atmos, 118(1), 73-84, doi:10.1029/2012jd018813.

Liu, H., D. J. Jacob, I. Bey, and R. M. Yantosca (2001), Constraints from 210Pb and 7Be on wet deposition and transport in a global three-dimensional chemical tracer model driven by

assimilated meteorological fields, Journal of Geophysical Research: Atmospheres, 106(D11), 12109-12128, doi:https://doi.org/10.1029/2000JD900839.

Luz, B., E. Barkan, M. L. Bender, M. H. Thiemens, and K. A. Boering (1999), Triple-isotope composition of atmospheric oxygen as a tracer of biosphere productivity, Nature, 400(6744), 547.

Meul, S., U. Langematz, P. Kröger, S. Oberländer-Hayn, and P. Jöckel (2018), Future changes in the stratosphere-to-troposphere ozone mass flux and the contribution from climate change and ozone recovery, Atmos. Chem. Phys., 18(10), 7721-7738, doi:10.5194/acp-18-7721-2018.

Murray, L. T., L. J. Mickley, J. O. Kaplan, E. D. Sofen, M. Pfeiffer, and B. Alexander (2014), Factors controlling variability in the oxidative capacity of the troposphere since the Last Glacial Maximum, Atmos Chem Phys, 14(7), 3589-3622, doi:10.5194/acp-14-3589-2014.

Olaguer, E. P., H. Yang, and K. K. Tung (1992), A Reexamination of the Radiative Balance of the Stratosphere, J Atmos Sci, 49(14), 1242-1263, doi:10.1175/1520-0469(1992)049<1242:Arotrb>2.0.Co;2.

Oleson, K. W., D. M. Lawrence, B. Gordon, M. G. Flanner, E. Kluzek, J. Peter, S. Levis, S. C. Swenson, E. Thornton, and J. Feddema (2010), Technical description of version 4.0 of the Community Land Model (CLM).

Olsen, M. A., A. R. Douglass, and T. B. Kaplan (2013), Variability of extratropical ozone stratosphere-troposphere exchange using microwave limb sounder observations, J Geophys Res-Atmos, 118(2), 1090-1099, doi:10.1029/2012jd018465.

Olsen, M. A., M. R. Schoeberl, and A. R. Douglass (2004), Stratosphere-troposphere exchange of mass and ozone, J Geophys Res-Atmos, 109(D24), doi:10.1029/2004jd005186.

Orbe, C., M. Holzer, and L. M. Polvani (2012), Flux distributions as robust diagnostics of stratosphere-troposphere exchange, *Journal of Geophysical Research: Atmospheres*, *117*(D1), doi:https://doi.org/10.1029/2011JD016455.

Ordonez, C., D. Brunner, J. Staehelin, P. Hadjinicolaou, J. A. Pyle, M. Jonas, H. Wernli, and A. S. H. Prevot (2007), Strong influence of lowermost stratospheric ozone on lower tropospheric background ozone changes over Europe, Geophys Res Lett, 34(7), doi:10.1029/2006gl029113.

Randel, W. J., and E. J. Jensen (2013), Physical processes in the tropical tropopause layer and their roles in a changing climate, Nat Geosci, 6(3), 169-176, doi:10.1038/ngeo1733.

Randel, W. J., M. Park, L. Emmons, D. Kinnison, P. Bernath, K. A. Walker, C. Boone, and H. Pumphrey (2010), Asian Monsoon Transport of Pollution to the Stratosphere, Science, 328(5978), 611-613, doi:10.1126/science.1182274.

Rayner, N. A., D. E. Parker, E. B. Horton, C. K. Folland, L. V. Alexander, D. P. Rowell, E. C. Kent, and A. Kaplan (2003), Global analyses of sea surface temperature, sea ice, and night marine air temperature since the late nineteenth century, J Geophys Res-Atmos, 108(D14), doi:10.1029/2002jd002670.

Rosenlof, K. H. (1995), Seasonal cycle of the residual mean meridional circulation in the stratosphere, J Geophys Res-Atmos, 100(D3), 5173-5191, doi:10.1029/94jd03122.

Schoeberl, M. R. (2004), Extratropical stratosphere-troposphere mass exchange, J Geophys Res-Atmos, 109(D13), doi:10.1029/2004jd004525.

Skerlak, B., M. Sprenger, and H. Wernli (2014), A global climatology of stratosphere-troposphere exchange using the ERA-Interim data set from 1979 to 2011, Atmos Chem Phys, 14(2), 913-937, doi:10.5194/acp-14-913-2014.

Solomon, S. (1999), Stratospheric ozone depletion: A review of concepts and history, Rev Geophys, 37(3), 275-316, doi:10.1029/1999rg900008.

Solomon, S., D. Kinnison, J. Bandoro, and R. Garcia (2015), Simulation of polar ozone depletion: An update, J Geophys Res-Atmos, 120(15), 7958-7974, doi:10.1002/2015jd023365.

Stohl, A., et al. (2003), Stratosphere-troposphere exchange: A review, and what we have learned from STACCATO, J Geophys Res-Atmos, 108(D12), doi:10.1029/2002jd002490.

Wang, M., and Q. Fu (2021), Stratosphere-troposphere exchange of air masses and ozone concentrations based on reanalyses and observations, J Geophys Res-Atmos.

Wang, M., Q. Fu, S. Solomon, R. H. White, and B. Alexander (2020), Stratospheric Ozone in the Last Glacial Maximum, J Geophys Res-Atmos, 125(21), doi:10.1029/2020jd032929.

Wernli, H., and M. Bourqui (2002), A Lagrangian "1-year climatology" of (deep) cross-tropopause exchange in the extratropical Northern Hemisphere, *Journal of Geophysical Research: Atmospheres*, *107*(D2), ACL 13-11-ACL 13-16, doi:https://doi.org/10.1029/2001JD000812.

World Meteorological Organization (1957). Meteorology—A three dimensional science: Second session of the Commission for Aerology. WMO Bulletin, IV(4), 134–138.

Yang, H., G. Chen, Q. Tang, and P. Hess (2016), Quantifying isentropic stratosphere-troposphere exchange of ozone, J Geophys Res-Atmos, 121(7), 3372-3387, doi:10.1002/2015jd024180.

Yeung, L. Y., L. T. Murray, P. Martinerie, E. Witrant, H. T. Hu, A. Banerjee, A. Orsi, and J. Chappellaz (2019), Isotopic constraint on the twentieth-century increase in tropospheric ozone, Nature, 570(7760), 224-+, doi:10.1038/s41586-019-1277-1.

Young, P. J., et al. (2013), Pre-industrial to end 21st century projections of tropospheric ozone from the Atmospheric Chemistry and Climate Model Intercomparison Project (ACCMIP), Atmos. Chem. Phys., 13(4), 2063-2090, doi:10.5194/acp-13-2063-2013.

Young, P. J., et al. (2018), Tropospheric Ozone Assessment Report: Assessment of global-scale model performance for global and regional ozone distributions, variability, and trends, Elementa-Science of the Anthropocene, 6, doi:10.1525/elementa.265

Table captions

Table 1. Annual-mean diabatic air mass fluxes across the upper isentropic boundary of the lowermost stratosphere, rate of change of the lowermost stratosphere air mass, and tropopause net, diabatic, and adiabatic air mass fluxes (10^9 kg s^{-1}), over the Northern hemisphere (NH) extratropics, the Southern hemisphere (SH) extratropics, the tropics, the extratropics, and the globe from the WACCM6 pre-industrial (PI) simulation and the Last Glacial Maximum (LGM) simulations with prescribed sea surface temperature (SST) from the PMIP3 models (LGM_{PMIP3}) and proxy data (LGM_{PROXY}). The upper isentropic boundary is determined by fitting to the tropical lapse rate tropopause. The fitted upper isentropic surfaces are 370 K, 361 K, 365 K in the PI, LGM_{PMIP3}, LGM_{PROXY}, respectively. Numbers in parentheses are relative changes for LGM versus PI, which are in bold representing statistically significant at 95% confidence level, according to the Student's t test, with degrees of freedom adjusted for autocorrelation.

Table 2. The same as Table 1 but for ozone fluxes (Tg $year^{-1}$), with an added term for negative of ozone net chemical source in the lowermost stratosphere (−CTO3) (positive indicates ozone net chemical sink in the lowermost stratosphere and vice versa).

Table 3. Global annual-mean diabatic ozone fluxes across the 380 K isentropic surfaces, rate of change of the lowermost stratosphere ozone mass (dO_3/dt), negative of ozone net chemical source in the lowermost stratosphere (−CTO3), and tropopause net, diabatic, and adiabatic ozone fluxes (Tg $year^{-1}$) in the PI, LGM_{PMIP3}, LGM_{PROXY} simulations, following Wang and Fu (2021) method.

Table 4. Global annual-mean tropospheric ozone burden, ozone lifetime, ozone chemical production rate, ozone chemical loss rate, ozone deposition flux, stratosphere-troposphere exchange (STE) of ozone derived from the present study, and the residual of tropospheric

ozone budget (i.e., the summation of tropospheric ozone production, loss, deposition, and ozone STE) in the WACCM6 MC, PI, LGM_{PMIP3}, and LGM_{PROXY} simulations. The tropospheric ozone sources (i.e., ozone production rate and ozone STE) and sinks (i.e., ozone loss rate and deposition) are shown as positive and negative values, respectively.

Figure captions

Figure 1. Schematic diagrams of the stratosphere-troposphere exchange of air masses and ozone concentrations for (a) Appenzeller et al. (1996), (b) Wang and Fu (2021), and (c) dynamic upper isentrope method (this study). The zero diabatic heating contour is indicated by the green dashed line. The blue solid lines in (a) and (c) are the 3.5 potential vorticity unit (PVU) tropopause, and the blue solid line in (b) is the 3.5 PVU tropopause combined with the lapse-rate tropopause in the tropics. The upper boundary of the lowermost stratosphere, represented as the red solid lines, are the 380 K isentrope in (a) and (b), and the fitted upper isentrope in (c). This fitted upper isentrope is determined by the best-fit isentrope (at a 1 K interval) for the lapse rate tropopause (blue dashed line in (c)) over the regions equatorward of the latitudes with zero tropopause diabatic heating. The tropics/extratropics boundaries in (a), (b), and (c) are defined as the cross points between 3.5 PVU tropopause and the 380 K isentrope, the zero diabatic heating at the tropopause (i.e., white vertical lines in (b)), and the zero diabatic heating at the fitted upper isentropic surfaces (i.e., black dashed vertical lines in (c)), respectively. The latitudes of the tropics/extratropics boundaries of each method in the PI are given in the upper right corners. The light blue shading indicates the extratropical lowermost stratosphere region, and the light red shading in (b) indicates the tropical lowermost

stratosphere region. Blue arrows indicate the tropopause net fluxes, and red arrows indicate the diabatic flux across the upper isentropic surfaces and the tropopause. Red wavy double-headed arrows represent the adiabatic flux across the tropopause; the red wavy double-headed arrows across the white vertical lines in (b) indicate the quasi-horizontal transport between the tropical and extratropical lowermost stratosphere, which are not part of the stratosphere-troposphere exchanges. The isentropic surfaces of 360, 340, 320, and 300 K are shown as red dashed lines, with the isentropic surface of 380 K also shown in (c) for reference.

Figure 2. The seasonal cycle of tropopause net (black solid lines), diabatic (black dashed lines), and adiabatic (black dash-dot lines) air mass (left) and ozone (right) fluxes over the Northern hemisphere extratropics (a and b), Southern hemisphere extratropics (c and d), the tropics (e and f), and the globe (g) from the WACCM6 pre-industrial simulation. Red solid lines represent the diabatic air mass (left) and ozone (right) fluxes across the fitted upper isentropic surface (i.e., 370 K isentrope). Blue solid lines represent the rate of change of the lowermost stratosphere air mass (left) and ozone mass (right). Green lines (left) represent negative of ozone net chemical source in the lowermost stratosphere (−CTO3) (positive indicates ozone net chemical sink in the lowermost stratosphere and vice versa). Over the tropics, only the tropopause net fluxes are shown in panels (e) and (f) since the tropopause adiabatic fluxes are zero, and the tropopause diabatic and net fluxes are the same.

Figure 3. Latitudinal distributions of annual-mean zonal-mean (a) adjusted diabatic heating (K day^{-1}), (b) isentropic density (kg m^{-2} K^{-1}), (c) ozone mass mixing ratio (ppm), and (d) pressure (hPa) at the fitted upper isentropic surfaces in the PI, LGM_{PMIP3}, and LGM_{PROXY}

simulations. Panels (e)-(h) are the corresponding changes in the LGM_{PMIP3} and LGM_{PROXY} relative to the PI simulation. Lines in panels (e)-(h) that are not shaded are statistically significant at 95% confidence level, according to the Student's t test, with degrees of freedom adjusted for autocorrelation.

Figure 4. The same as Figure 3 but for longwave (left) and shortwave (right) heating rates (K day $^{-1}$) at the fitted upper isentropic surfaces. No adjustment is applied to the longwave and shortwave heating rates.

Figure 5. Relative differences (gray colors) in annual-mean air mass (left) and ozone (right) diabatic fluxes at the fitted upper isentropic surfaces over the Northern hemisphere extratropics (a and b), Southern hemisphere extratropics (c and d), the tropics (e and f), and the globe (g) for LGM_{PMIP3} versus PI and LGM_{PROXY} versus PI. Red, blue, orange, and cyan colors indicate the relative differences of diabatic fluxes due to the differences in diabatic heating, isentropic density, ozone mass mixing ratio, and extratropics-tropics boundaries. The bars with the slant lines indicate the relative differences are statistically significant at 95% confidence level, according to the Student's t test, with degrees of freedom adjusted for autocorrelation.

Table 1. Annual-mean diabatic air mass fluxes across the upper isentropic boundary of the lowermost stratosphere, rate of change of the lowermost stratosphere air mass, and tropopause

net, diabatic, and adiabatic air mass fluxes (10^9 kg s^{-1}), over the Northern hemisphere (NH) extratropics, the Southern hemisphere (SH) extratropics, the tropics, the extratropics, and the globe from the WACCM6 pre-industrial (PI) simulation and the Last Glacial Maximum (LGM) simulations with prescribed sea surface temperature (SST) from the PMIP3 models (LGM_{PMIP3}) and proxy data (LGM_{PROXY}). The upper isentropic boundary is determined by fitting to the tropical lapse rate tropopause. The fitted upper isentropic surfaces are 370 K, 361 K, 365 K in the PI, LGM_{PMIP3}, LGM_{PROXY}, respectively. Numbers in parentheses are relative changes for LGM versus PI, which are in bold representing statistically significant at 95% confidence level, according to the Student's t test, with degrees of freedom adjusted for autocorrelation.

(a) PI

	NH extratropics	SH extratropics	Tropics	Extratropics	Global
370K diabatic	-10.9	-8.5	19.5	-19.5	0
dM/dt	0	0	0	0	0
Tropopause net	-10.9	-8.5	19.5	-19.4	0
Tropopause diabatic	-36	-27.6	19.5	-63.6	-44.2
Tropopause adiabatic	25.1	19.1	0	44.2	44.2

(b) LGM_{PMIP3}

	NH extratropics		SH extratropics		Tropics		Extratropics		Global	
361K diabatic	-11.7	**(7.1%)**	-8.5	(-0.3%)	20.2	**(3.9%)**	-20.2	**(3.9%)**	0	
dM/dt	0		0		0		0		0	
Tropopause net	-11.7	**(7.1%)**	-8.5	(-0.3%)	20.2	**(3.9%)**	-20.2	**(3.9%)**	0	
Tropopause diabatic	-36.4	**(1.2%)**	-27	**(-2.3%)**	20.2	**(3.9%)**	-63.4	(-0.3%)	-43.2	**(-2.2%)**
Tropopause adiabatic	24.7	**(-1.4%)**	18.5	**(-3.2%)**	0		43.2	**(-2.2%)**	43.2	**(-2.2%)**

(c) LGM_{PROXY}

	NH extratropics		SH extratropics		Tropics		Extratropics		Global	
365K diabatic	-11.5	**(5.4%)**	-8.4	**(-1.5%)**	19.9	**(2.4%)**	-19.9	**(2.4%)**	0	
dM/dt	0		0		0		0		0	
Tropopause net	-11.5	**(5.6%)**	-8.4	**(-1.5%)**	19.9	**(2.4%)**	-19.9	**(2.5%)**	0	
Tropopause diabatic	-36.7	**(2%)**	-27.9	(1.1%)	19.9	**(2.4%)**	-64.7	**(1.6%)**	-44.7	**(1.3%)**
Tropopause adiabatic	25.2	(0.5%)	19.5	**(2.2%)**	0		44.7	(1.2%)	44.7	(1.2%)

Table 2. The same as Table 1 but for ozone fluxes (Tg $year^{-1}$), with an added term for negative of ozone net chemical source in the lowermost stratosphere (−CTO3) (positive indicates ozone net chemical sink in the lowermost stratosphere and vice versa).

(a) PI

	NH extratropics	SH extratropics	Tropics	Extratropics	Global
370K diabatic	-262.4	-196.1	77.8	-458.5	-380.7
dO_3/dt	0.1	-0.1	0	0.1	0.1
−CTO3	8.3	5.2	0	13.5	13.5
Tropopause net	-253.9	-190.9	77.8	-444.9	-367.1
Tropopause diabatic	-262.3	-189.3	77.8	-451.6	-373.8
Tropopause adiabatic	8.4	-1.7	0	6.7	6.7

(b) LGM_{PMIP3}

	NH extratropics		SH extratropics		Tropics		Extratropics		Global	
361K diabatic	-214	**(-18.4%)**	-151.3	**(-22.9%)**	59.6	**(-23.3%)**	-365.3	**(-20.3%)**	-305.6	**(-19.7%)**
dO_3/dt	-0.3		-0.1		0		-0.4		-0.4	
−CTO3	8.9	**(7.7%)**	6	**(14%)**	0		14.9	**(10.1%)**	14.9	**(10.1%)**
Tropopause net	-205.4	**(-19.1%)**	-145.4	**(-23.9%)**	59.6	**(-23.3%)**	-350.7	**(-21.2%)**	-291.1	**(-20.7%)**
Tropopause diabatic	-212.4	**(-19%)**	-144.3	**(-23.8%)**	59.6	**(-23.3%)**	-356.7	**(-21%)**	-297	**(-20.5%)**
Tropopause adiabatic	7	(-16.7%)	-1.1	(-36.9%)	0		5.9	(-11.7%)	5.9	(-11.7%)

(c) LGM_{PROXY}

	NH extratropics		SH extratropics		Tropics		Extratropics		Global	
365K diabatic	-229	**(-12.7%)**	-164.5	**(-16.1%)**	63.5	**(-18.4%)**	-393.5	**(-14.2%)**	-330	**(-13.3%)**
dO_3/dt	-0.2		0		0		-0.2		-0.2	
−CTO3	11.1	**(33.7%)**	7.1	**(36.1%)**	0		18.2	**(34.7%)**	18.2	**(34.7%)**
Tropopause net	-218.2	**(-14.1%)**	-157.3	**(-17.6%)**	63.5	**(-18.4%)**	-375.5	**(-15.6%)**	-312	**(-15%)**
Tropopause diabatic	-227.1	**(-13.4%)**	-157	**(-17%)**	63.5	**(-18.4%)**	-384.1	**(-14.9%)**	-320.6	**(-14.2%)**
Tropopause adiabatic	8.9	(6.2%)	-0.3	**(-83.8%)**	0		8.6	(28.6%)	8.6	(28.6%)

Table 3. Global annual-mean diabatic ozone fluxes across the 380 K isentropic surfaces, rate of change of the lowermost stratosphere ozone mass (dO_3/dt), negative of ozone net chemical source in the lowermost stratosphere (−CTO3), and tropopause net, diabatic, and adiabatic ozone

fluxes (Tg year^{-1}) in the PI, LGM_{PMIP3}, LGM_{PROXY} simulations, following Wang and Fu (2021) method.

	PI	LGM_{PMIP3}	LGM_{PROXY}
380K diabatic	-363.4	-278.9	-305.8
dO_3/dt	0	-0.6	-0.2
−CTO3	-3.9	-7.8	-2.4
Tropopause net	-367.3	-287.3	-308.4
Tropopause diabatic	-368.1	-292.7	-318.2
Tropopause adiabatic	0.8	5.4	9.8

Table 4. Global annual-mean tropospheric ozone burden, ozone lifetime, ozone chemical production rate, ozone chemical loss rate, ozone deposition flux, stratosphere-troposphere exchange (STE) of ozone derived from the present study, and the residual of tropospheric ozone

budget (i.e., the summation of tropospheric ozone production, loss, deposition, and ozone STE) in the WACCM6 MC, PI, LGM_{PMIP3}, and LGM_{PROXY} simulations. The tropospheric ozone sources (i.e., ozone production rate and ozone STE) and sinks (i.e., ozone loss rate and deposition) are shown as positive and negative values, respectively.

	MC	PI	LGM_{PMIP3}	LGM_{PROXY}
Tropospheric ozone burden (Tg)	303.8	190.6	134.9	136.8
Ozone lifetime (day)	25.4	29.8	35.0	34.4
Ozone production rate (Tg $year^{-1}$)	4103.8	1916.9	1071.3	1086.0
Ozone loss rate (Tg $year^{-1}$)	-3581.6	-1885.5	-1089.6	-1136.0
Ozone deposition flux (Tg $year^{-1}$)	-786.1	-448.8	-318.0	-314.6
Ozone STE (Tg $year^{-1}$)	364.0	367.1	291.1	312.0
Residual (Tg $year^{-1}$)	100.1	-50.4	-45.1	-52.6

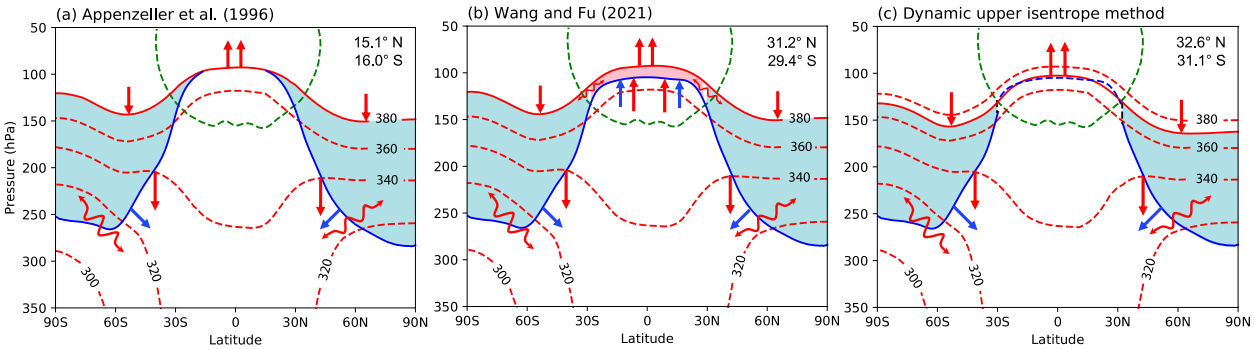

Figure 1. Schematic diagrams of the stratosphere-troposphere exchange of air masses and ozone concentrations for (a) Appenzeller et al. (1996), (b) Wang and Fu (2021), and (c) dynamic upper isentrope method (this study). The zero diabatic heating contour is indicated by the green dashed line. The blue solid lines in (a) and (c) are the 3.5 potential vorticity unit (PVU) tropopause, and the blue solid line in (b) is the 3.5 PVU tropopause combined with the lapse-rate tropopause in the tropics. The upper boundary of the lowermost stratosphere, represented as the red solid lines, are the 380 K isentrope in (a) and (b), and the fitted upper isentrope in (c). This fitted upper isentrope is determined by the best-fit isentrope (at a 1 K interval) for the lapse rate tropopause (blue dashed line in (c)) over the regions equatorward of the latitudes with zero tropopause diabatic heating. The tropics/extratropics boundaries in (a), (b), and (c) are defined as the cross points between 3.5 PVU tropopause and the 380 K isentrope, the zero diabatic heating at the tropopause (i.e., white vertical lines in (b)), and the zero diabatic heating at the fitted upper isentropic surfaces (i.e., black dashed vertical lines in (c)), respectively. The latitudes of the tropics/extratropics boundaries of each method in the PI are given in the upper right corners. The light blue shading indicates the extratropical lowermost stratosphere region, and the light red shading in (b) indicates the tropical lowermost stratosphere region. Blue arrows indicate the tropopause net fluxes, and red arrows indicate the diabatic flux across the upper isentropic surfaces and the tropopause. Red wavy double-headed arrows represent the adiabatic flux across the tropopause; the red wavy double-headed arrows across the white vertical lines in (b) indicate the quasi-horizontal transport between the tropical and extratropical lowermost stratosphere, which are not part of the stratosphere-troposphere exchanges. The isentropic surfaces of 360, 340, 320, and 300 K are shown as red dashed lines, with the isentropic surface of 380 K also shown in (c) for reference.

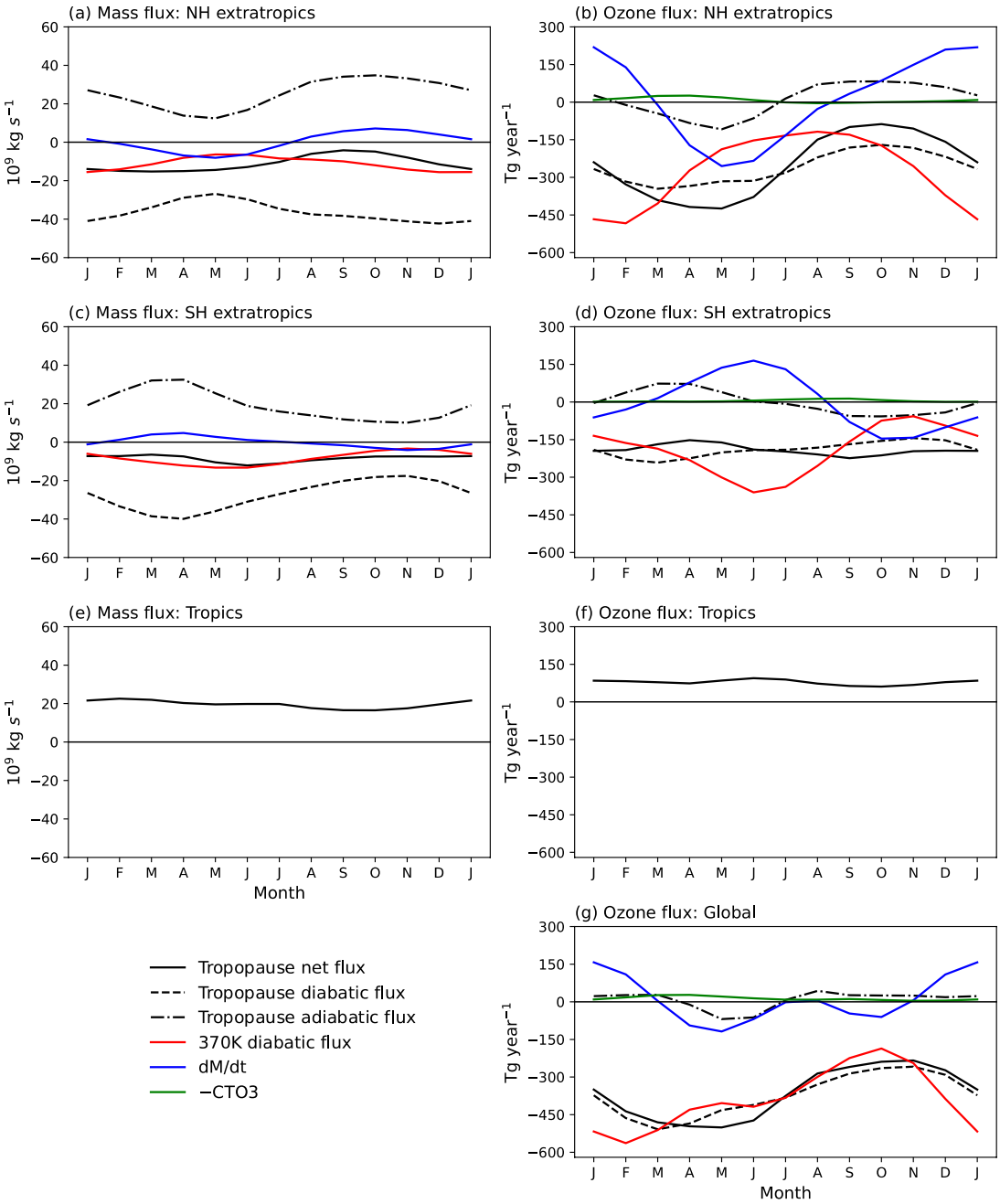

Figure 2. The seasonal cycle of tropopause net (black solid lines), diabatic (black dashed lines), and adiabatic (black dash-dot lines) air mass (left) and ozone (right) fluxes over the Northern hemisphere extratropics (a and b), Southern hemisphere extratropics (c and d), the tropics (e and f), and the globe (g) from the WACCM6 pre-industrial simulation. Red solid lines represent the diabatic air mass (left) and ozone (right) fluxes across the fitted upper isentropic surface (i.e., 370 K isentrope). Blue solid lines represent the rate of change of the lowermost stratosphere air mass (left) and ozone mass (right). Green lines (left) represent negative of ozone net chemical source in the lowermost stratosphere (−CTO3) (positive indicates ozone net chemical sink in the lowermost stratosphere and vice versa). Over the tropics, only the tropopause net fluxes are shown in panels (e) and (f) since the tropopause adiabatic fluxes are zero, and the tropopause diabatic and net fluxes are the same.

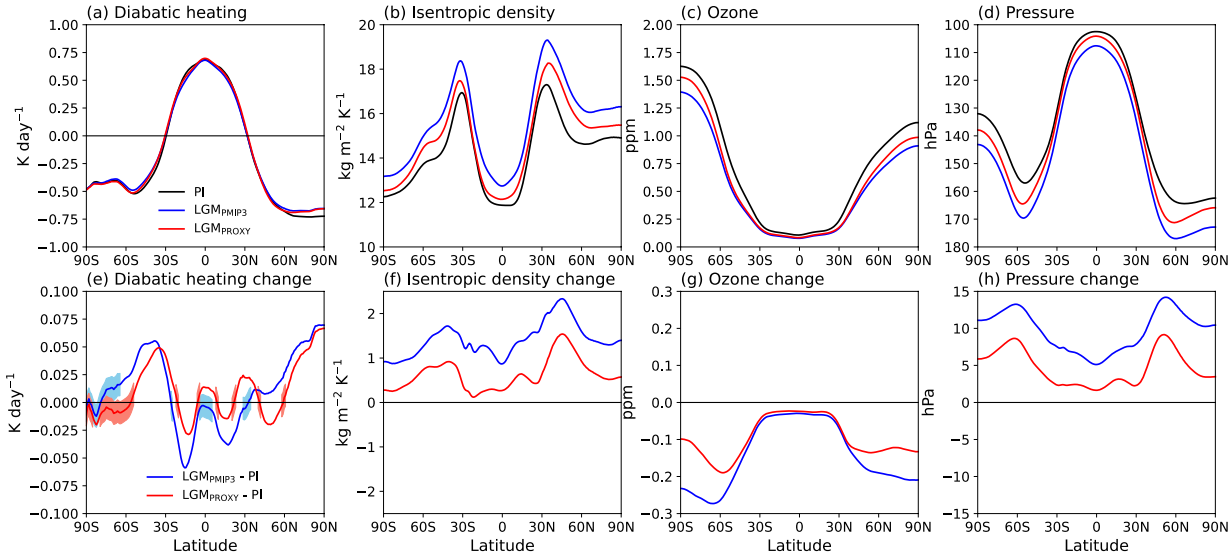

Figure 3. Latitudinal distributions of annual-mean zonal-mean (a) adjusted diabatic heating (K day^{-1}), (b) isentropic density (kg m^{-2} K^{-1}), (c) ozone mass mixing ratio (ppm), and (d) pressure (hPa) at the fitted upper isentropic surfaces in the PI, LGM$_{PMIP3}$, and LGM$_{PROXY}$ simulations. Panels (e)-(h) are the corresponding changes in the LGM$_{PMIP3}$ and LGM$_{PROXY}$ relative to the PI simulation. Lines in panels (e)-(h) that are not shaded are statistically significant at 95% confidence level, according to the Student's t test, with degrees of freedom adjusted for autocorrelation.

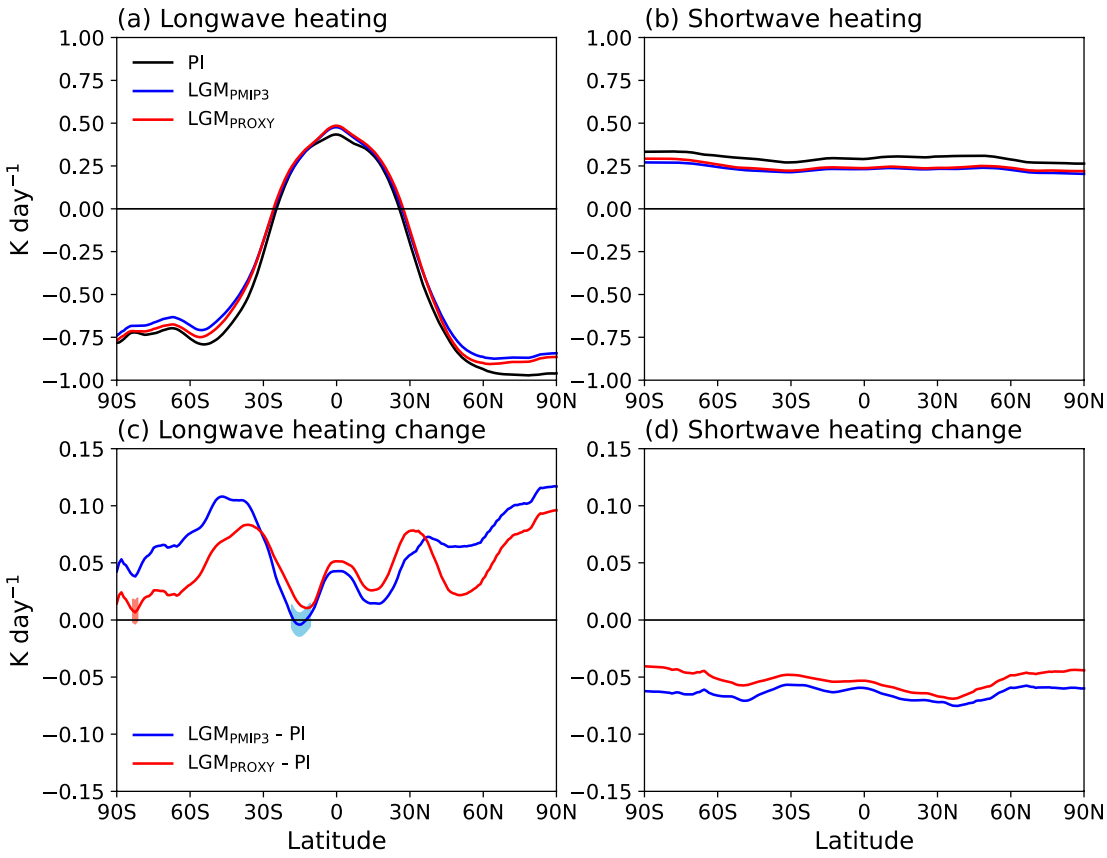

Figure 4. The same as Figure 3 but for longwave (left) and shortwave (right) heating rates (K day $^{-1}$) at the fitted upper isentropic surfaces. No adjustment is applied to the longwave and shortwave heating rates.

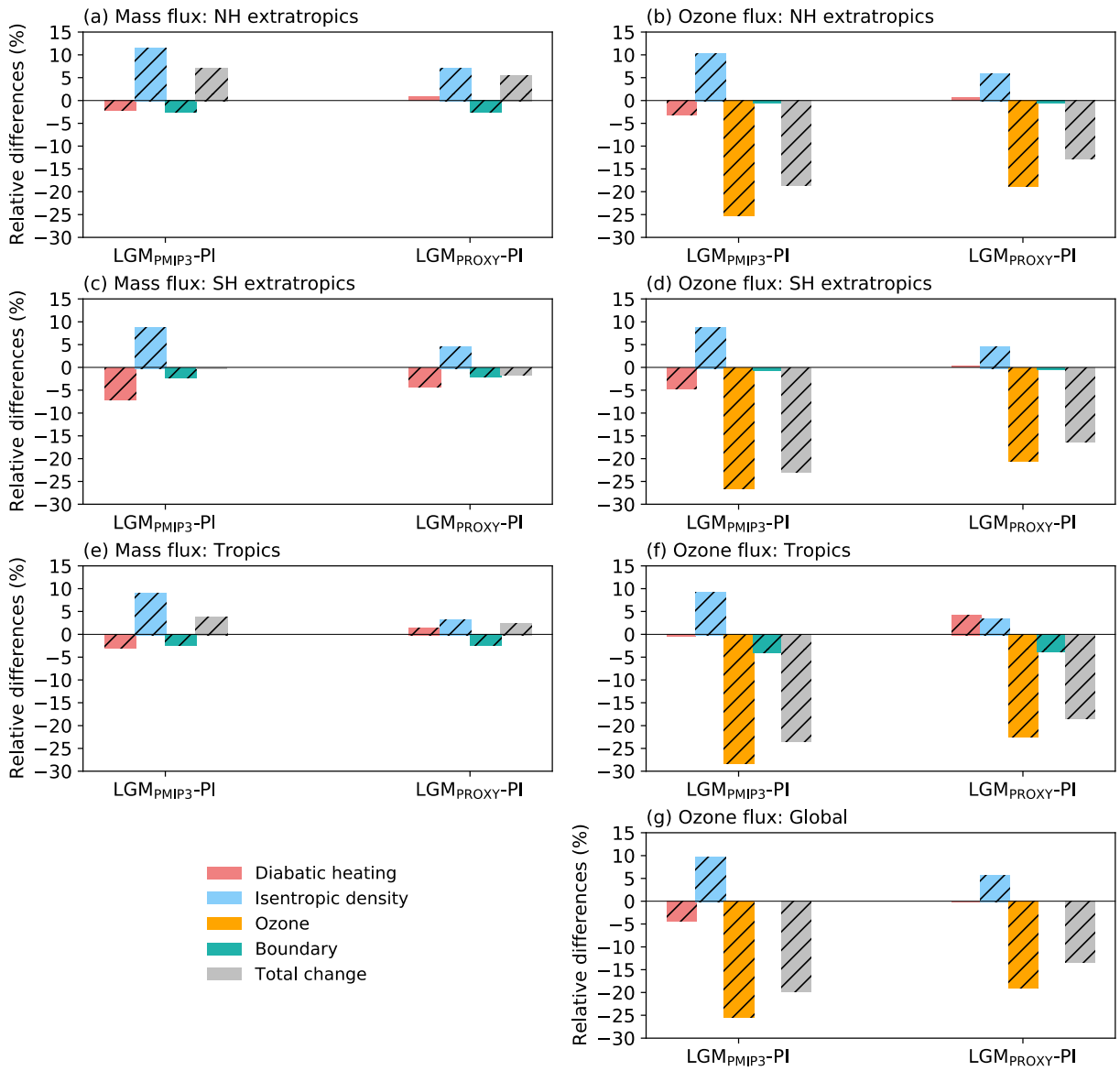

Figure 5. Relative differences (gray colors) in annual-mean air mass (left) and ozone (right) diabatic fluxes at the fitted upper isentropic surfaces over the Northern hemisphere extratropics (a and b), Southern hemisphere extratropics (c and d), the tropics (e and f), and the globe (g) for LGM_{PMIP3} versus PI and LGM_{PROXY} versus PI. Red, blue, orange, and cyan colors indicate the relative differences of diabatic fluxes due to the differences in diabatic heating, isentropic density, ozone mass mixing ratio, and extratropics-tropics boundaries. The bars with the slant lines indicate the relative differences are statistically significant at 95% confidence level, according to the Student's t test, with degrees of freedom adjusted for autocorrelation.

Figure 1.

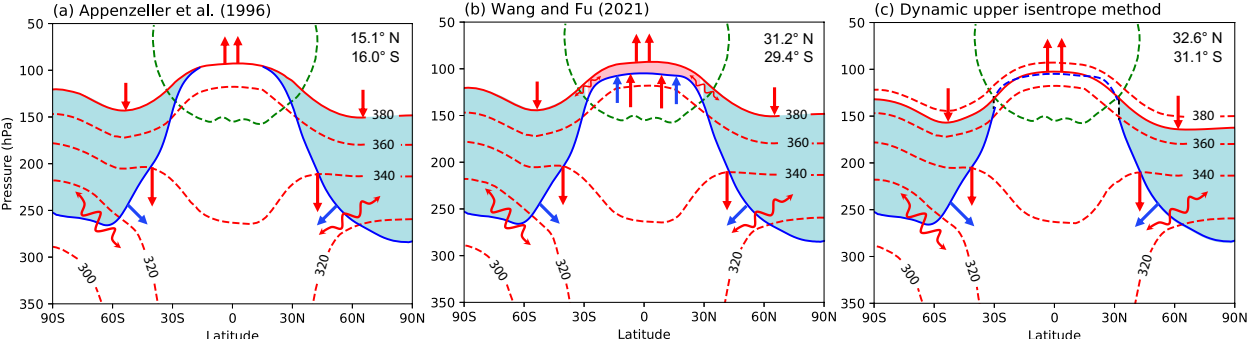
(a) Appenzeller et al. (1996)
15.1° N
16.0° S
(b) Wang and Fu (2021)
31.2° N
29.4° S
(c) Dynamic upper isentrope method
32.6° N
31.1° S
Pressure (hPa)
50
100
150
200
250
300
350
380
360
340
320
300
90S
60S
30S
0
30N
60N
90N
Latitude

Figure 2.

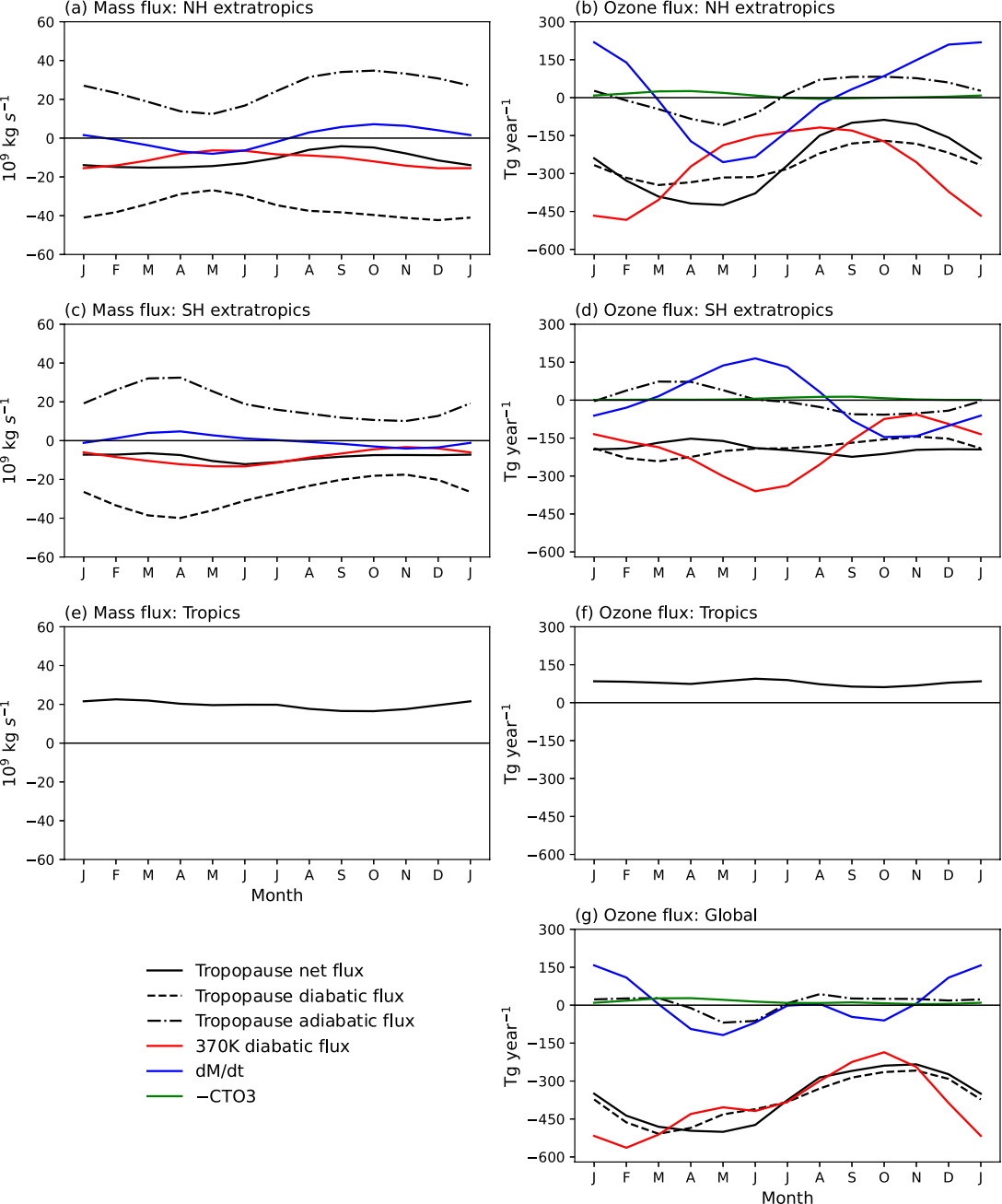
(a) Mass flux: NH extratropics
(b) Ozone flux: NH extratropics
(c) Mass flux: SH extratropics
(d) Ozone flux: SH extratropics
(e) Mass flux: Tropics
(f) Ozone flux: Tropics
(g) Ozone flux: Global
10^9 kg s^{-1}
Tg year^{-1}
J F M A M J J A S O N D J
Month
Tropopause net flux
Tropopause diabatic flux
Tropopause adiabatic flux
370K diabatic flux
dM/dt
−CTO3

Figure 3.

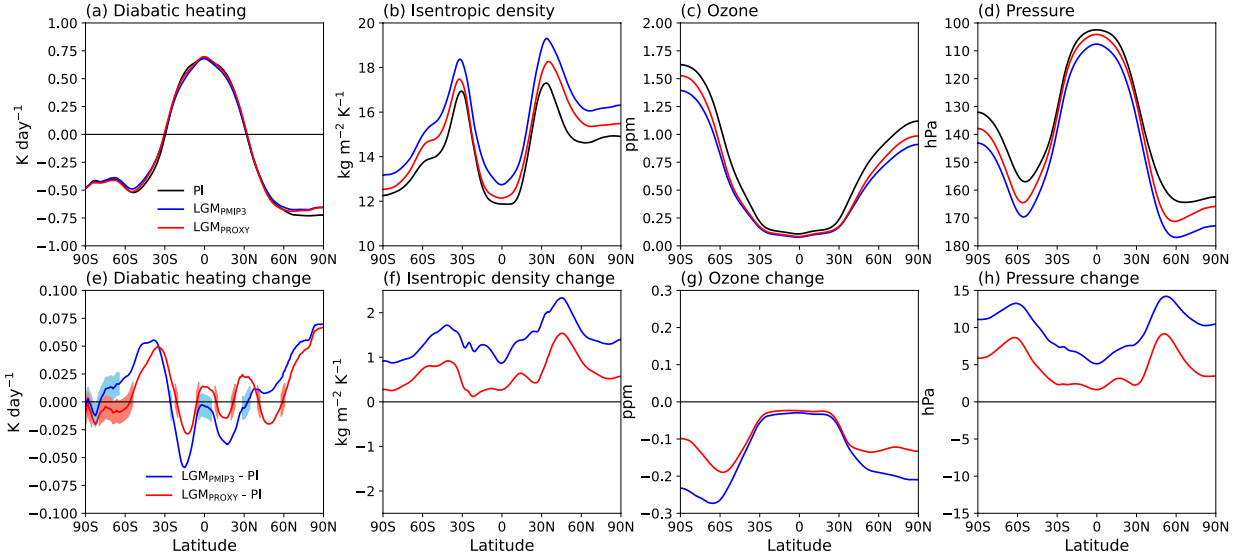
(a) Diabatic heating
K day^{-1}
PI
LGM$_{PMIP3}$
LGM$_{PROXY}$
(b) Isentropic density
kg m^{-2} K^{-1}
(c) Ozone
ppm
(d) Pressure
hPa
(e) Diabatic heating change
K day^{-1}
LGM$_{PMIP3}$ - PI
LGM$_{PROXY}$ - PI
(f) Isentropic density change
kg m^{-2} K^{-1}
(g) Ozone change
ppm
(h) Pressure change
hPa
90S 60S 30S 0 30N 60N 90N
Latitude

Figure 4.

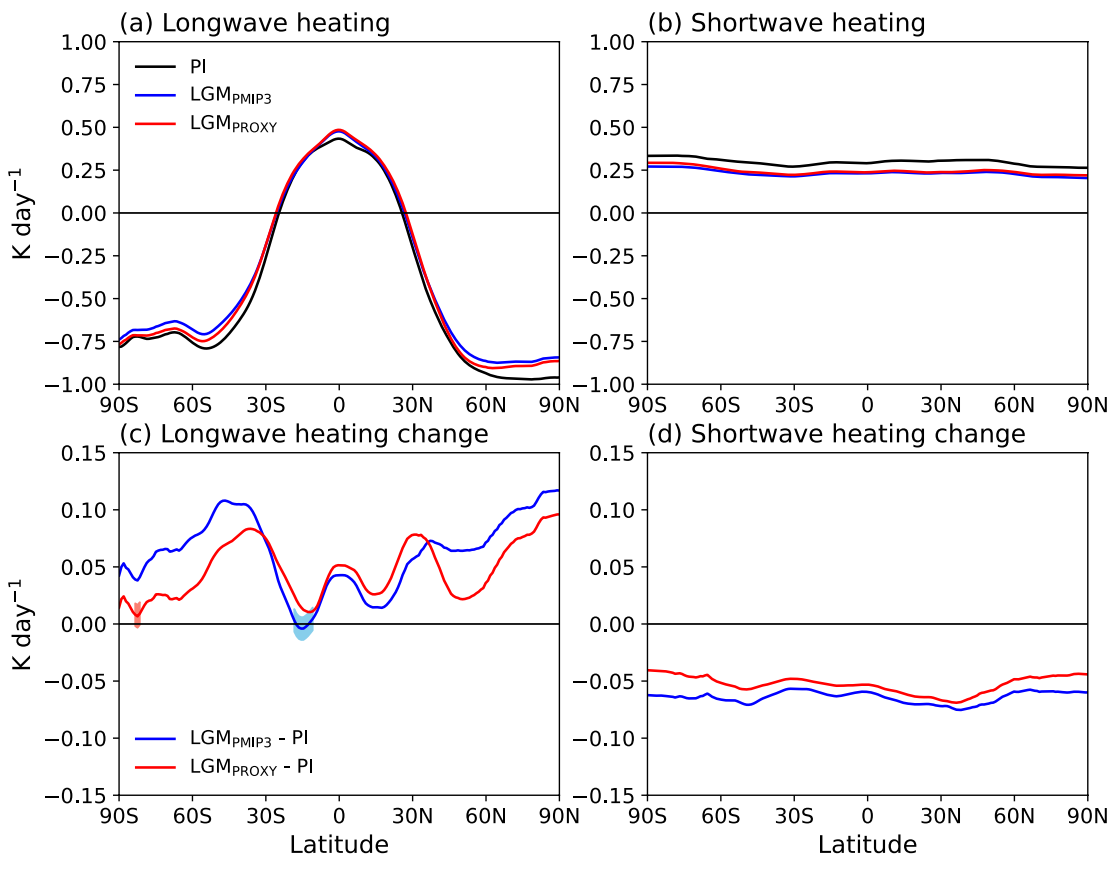
(a) Longwave heating
(b) Shortwave heating
(c) Longwave heating change
(d) Shortwave heating change
PI
LGM$_{PMIP3}$
LGM$_{PROXY}$
LGM$_{PMIP3}$ - PI
LGM$_{PROXY}$ - PI
K day^{-1}
Latitude
90S
60S
30S
0
30N
60N
90N
1.00
0.75
0.50
0.25
0.00
−0.25
−0.50
−0.75
−1.00
0.15
0.10
0.05
0.00
−0.05
−0.10
−0.15

Figure 5.

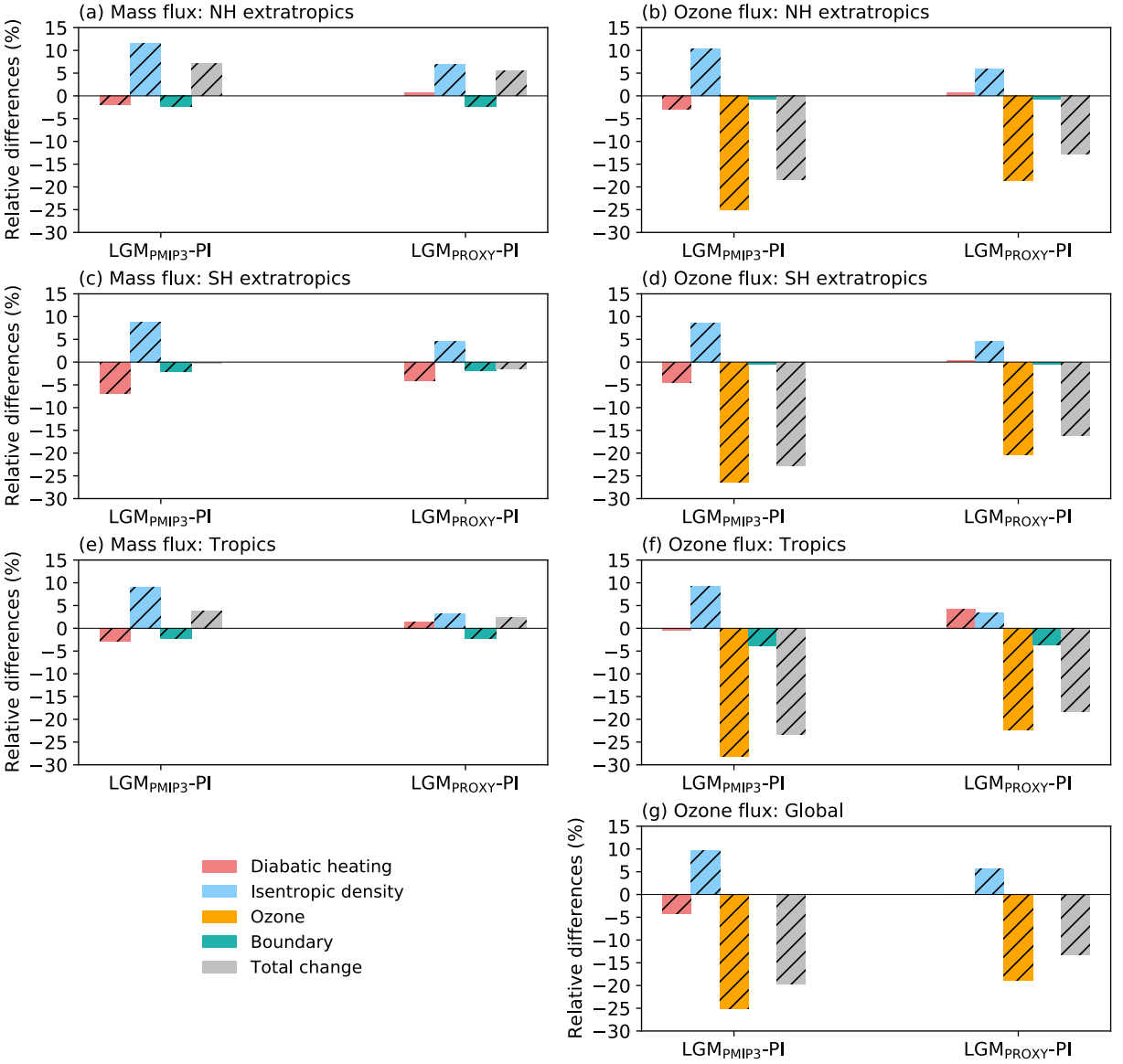
(a) Mass flux: NH extratropics
(b) Ozone flux: NH extratropics
(c) Mass flux: SH extratropics
(d) Ozone flux: SH extratropics
(e) Mass flux: Tropics
(f) Ozone flux: Tropics
(g) Ozone flux: Global
Relative differences (%)
15
10
5
0
−5
−10
−15
−20
−25
−30
LGMPMIP3-PI
LGMPROXY-PI
Diabatic heating
Isentropic density
Ozone
Boundary
Total change